Nanoscale

Accepted Manuscript

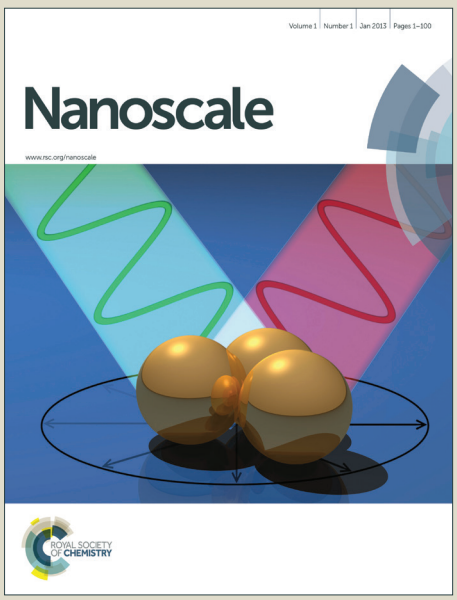

ROYAL SOCIETY OF CHEMISTRY

www.rsc.org/nanoscale

Nanoscale

RSCPublishing

COMMUNICATION

Quasi-3D Gold Nanoring Cavity Arrays with High-Density Hot-Spots for SERS Applications *via* Nanosphere Lithography

27830030Cite this: DOI: 10.1039/x0xx00000x

Received ooth January 2012,
Accepted ooth January 2012

DOI: 10.1039/x0xx00000x

www.rsc.org/

Chi-Chih Ho[a,c], Ke Zhao[b] and Tze-Yang Lee[a]*

a) *Department of Engineering and System science, National Tsing Hua University, Hsinchhu, Taiwan.*
b) *Department of Physics and Astronomy, and Laboratory for Nanophotonics, Rice University, 6100 Main Street, Houston, Texas 77005, United States*
c) *Taiwan international graduation program, Nanoscience and technology program, Institute of chemistry, Academia Sinica, Taipei, Taiwan*

Large-scale ordered arrays with dense hot spots are highly desirable substrates for practical applications, such as surface enhanced Raman scattering (SERS). In the past decades, most works focused on using lateral gaps between two metal structures. However, the strength and density of the generated hot spots are limited to a 2D arrangement of nanostructures. In this work, we present a novel quasi-3D nanoring cavity structure which contains a nanoring and a nanopillar in a nanohole. The fabrication is based on nanosphere lithography incorporated with dry etching and gold coating. Gold nanostructures with one layer (nanohole), 2 layers (nanohole + nanodisc), and 3 layers (nanohole + nanoring + nanopillar) were successfully fabricated and compared. The SERS performance of the 3-layered nanostructures is about two orders of magnitude higher than the others. Finite-difference time-domain (FDTD) simulations show that incorporating nanopillars and nanorings into a nanohole array not only significantly increases density of hot spots but also achieves stronger electromagnetic field enhancements compared to a nanohole array. The simple fabrication of multilayered quasi-3D nanostructures provides a large-area and high efficient SERS substrates for biological and chemical applications.

Tremendous enhancement of Raman scattering spectra is observed when molecules are placed in the vicinity of metallic nanoparticles, which is recognized as surface-enhanced Raman scattering (SERS).[1] The locally enhanced electric field resulting from excitation of surface plasmons on metal nanostructures contributes dominantly to SERS. SERS not only provides high-resolution fingerprint information of molecules but also enables single molecule detection with an optimal geometry of the substrate.[2-4] Due to its unique advantages in molecular characterization, SERS has become a powerful tool for analyzing small concentration of molecules, label-free molecule probing,[5] and disease diagnosis.[6] SERS-based lab-on-chip sensing devices are usually relied on reproducible, inexpensive and large-scale fabrication. Metallic nanostructured array-typed SERS platforms are becoming desirable because of better uniformity and convenience, compared to nanoparticles suspended solutions. To date, diverse methods have been introduced to pattern ordered arrays on flat substrates, such as deep ultra-violet lithography, focus ion beam lithography, electron beam lithography,[7] and nanosphere lithography (NSL).[8] Among them, NSL offers a practical and cost-effective route to large-area array fabrications. By using a monolayer of air/water interfacial assembly as a NSL mask, an inexpensive and facile fabrication for high quality arrays in a scalable manner is achievable. An overview of the fabrication of nanohole arrays using NSL has been reported in the literature.[9]

Previous works on 2D ordered arrays of nanopillar,[10] nanohole,[11,12] nanodisc[13] and nanoring[14] with deposition of single-layered gold or silver have been demonstrated to display applicable and uniform SERS effects. In recent efforts, more complicated structures toward 3D such as a "particle in hole"[15], a "particle in bowl"[16] and "particle in cavity"[17] were fabricated to improve the efficiency of SERS. Benefiting from the coupling between metal nanoparticles, these composite nanostructures can provide further field enhancement for SERS application. Quasi-3D structures composed of nanoholes and nanodisks, similar to our two-layered structure, were also fabricated for quantitative multispectral biosensing.[18] A recent review paper by Wei et al. provided a broad overview of the progresses on the development of SERS substrates.[19] In this study, we present a novel fabrication of NSL for obtaining a new SERS substrate with arrays of dense hot spots in a 3D arrangement. By merely exchanging the NSL procedures of the nanohole fabrication without adding other complicated steps, we can create a new architecture of multilayered arrays. The structure of a unit cell consists of a

nanopillar surrounded by a nanoring cavity and dressed at the center of a nanohole. Similar systems to nanoring cavities have received great attention in recent studies for its potential applications on plasmonic-based sensing,[20-22] photovoltaic,[23] and negative refractive index at visible frequencies.[24] To characterize the average SERS effect for practical applications, the analytic enhancement factor (AEF) were calculated using previously established methods.[7,25] In our SERS experiment, the AEF of the gold nanoring cavity arrays could be easily tuned up to 10^5 by merely controlling the thickness of the gold layer. The value of AEF is about two orders of magnitude higher than previously studied nanohole-based arrays with similar dimensions.[11,13] The physical mechanism of the enhancement of AEF for the multilayered systems is investigated by FDTD simulations. The simulation results clearly show that multilayered arrays effectively concentrate optical fields into nanoholes and generate more hot spots. Our novel method presents a high-throughput, inexpensive, and robust fabrication on periodic arrays, which can be readily integrated into a broad range of lab-on-chip devices.

Three types of periodic arrays were fabricated through NSL in this work and compared for SERS performance. The first type is a nanohole array without any structure inside holes. The second type is produced by the deposition of gold thin film onto a nanohole-templated substrate, which forms a two-layered structure with a nanodisc in each nanohole. For simplicity, it is given a name of "nanohole+disc".[26] The third type is a three-layered nanostructure composes of nanohole network on the top and a central nanopillar with a nanoring embedded in each nanohole, which is given a descriptive name of "nanoring cavity". Fig. 1 schematically shows the fabrication procedures of nanohole, nanohole+disc and nanoring cavity arrays using NSL, respectively. At first, 10wt% of PS NSs was mixed with ethanol (1:1 by volume), followed by introducing them onto water surface via a conduit. The spheres were then self-assembled at air/water interface. Water replacement was conducted several times to remove redundant sphere, ensuring a monolayer fabrication. After draining out water, a monolayer of self-assembled PS NSs array was placed on a hydrogen silsesquioxane (HSQ) layer in a hexagonally closed-packed arrangement as shown in Fig. 1(A). Then the diameters of PS NSs were reduced by oxygen plasma etching. HSQ, known as a spin-on glass, was chosen because of its etching selectivity to O_2 and CF_4 plasma. For the fabrication of a nanohole array, gold was deposited on a PS NSs-templated substrate, followed by removal of PS NSs, which can be seen in Fig. 1(A) to (A2). Procedures shown in Fig. 1(B) to (B2) are the fabrication of a nanohole+disc array using hole-mask colloidal lithography (HCL).[27] A thin layer of Cr was evaporated on a PS NSs array as a mask against CF_4 plasma (Fig. 1(B)). After removal of PS NSs, CF_4 reactive ion etching (RIE) was conducted vertically to perforate nanoholes on HSQ layer. After the deposition of gold thin film onto the nanohole-templated substrate, an array of nanohole+disc appeared. To obtain a nanoring cavity array, we reversed the steps of HCL as shown in Fig. 1(B1) and (B2). Thus the preserved PS NSs prevented the central area from RIE. The exposed region outside the central area, where was not fully protected by PS NSs, was etched leaving a ring-shape well. After etching and removal of PS NSs, the structure became a nanopillar located at the center of each nanohole as shown in Fig. 1(C1) and (C2). Then a nanoring cavity array was obtained by the following deposition of gold (Fig. 1(C3)). Consequently, three types of periodic arrays with evolving structural complexity were fabricated. All of these arrays have well-defined geometries. The periods of arrays were controlled by the diameters of starting PS NS. The inner and outer diameters of a nanoring cavity were controlled by the working time of O_2 and CF_4 RIE. The period and the outer diameters of all arrays were maintained at 500 nm and 370 nm in this work.

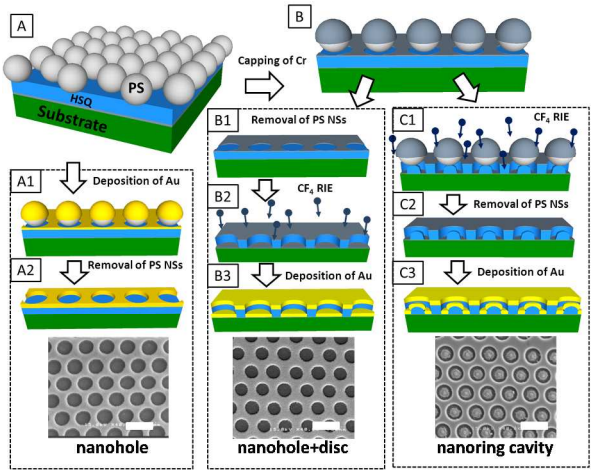

Fig. 1 Fabrication procedures to produce three types of periodic arrays. (A) A starting array of PS NSs on a HSQ coated substrate. (B) Capping of a Cr layer on PS NSs and exposed HSQ surface as a mask. (A1) to (A2) are the fabrication procedures of a nanohole array. (B1) to (B3) presents the fabrication of HCL for obtaining a nanohole+disc array. By exchanging the step of (B2) to (B1), i.e. doing the CF_4 RIE prior to the removal of PS NSs, the new sequence of (C1) to (C3) creates a nanoring cavity array. The scale bars in three SEM images are 600 nm.

Precise shapes of our fabricated structures were measured by scanning electron microscopy (SEM) and atomic force microscopy (AFM). Fig. 2(A) shows the SEM image of a hexagonal-packed nanoring cavity array with 55-nm-thick gold deposition. From the SEM image, the outer diameters, inner diameters, and the period were read as 370, 216 and 500 nm, respectively. The topography of nanoring cavities was acquired using atomic AFM with an ultra-sharp tip. The solid line in Fig. 2(B) denotes the averaged AFM line profile from the cross sections of several nanoring cavity unit cells. From the AFM analysis, the thickness of the HSQ layer and the effective height of the central pillar were estimated to be 95 nm and 60 nm on average, respectively. Fig. 2(C) presents a bird-eye-view of an SEM image of a nanoring cavity array. This confirms that each nanoring cavity unit cell consists of a central pillar surround by a ring. Fig. 2 displays the quality of

the structure which is nearly comparable to patterns produced by programmable lithography such as electron beam lithography.

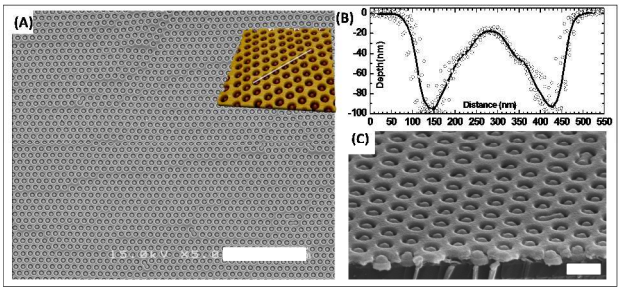

Fig. 2 (A) SEM image and AFM topography (inset) of a nanoring cavity array. The scale bar in the SEM image is 6 μm. (B) The open dots denote the line profiles of the cross sections corresponding to the white line in the inset of Fig. 2(A). The black solid line is the averaged profile fitted from several randomly-selected nanoring cavity unit cells. (C) A bird-eye-view SEM image of a nanoring cavity array. The scale bar is 600 nm.

In order to understand the plasmonic properties of the arrays, we measured and simulated the reflection spectra for three types of periodic arrays, namely, nanohole, nanohole+disc and nanoring cavity. In our SERS experiment, the samples were immerged in a liquid environment. So the environment for measurements and simulations of reflection spectra was also taken as water. The FDTD simulations were performed with commercial software (Lumerical FDTD solution). Fig. 3 shows the comparison of reflection spectra between experiments and simulations. Fano-like resonances supported by a nanohole+disc array and a nanoring cavity array were observed in experiments within the wavelength range from 600 nm to 650 nm, which were qualitatively agreed with FDTD simulation results. These Fano-like resonances occur due to coupling of the localized surface plasmon resonance (LSPR) of nanostructures in arrays and the Bloch-wave surface plasmon polaritons (BW-SPP) supported by periodic arrays.[28,29] The FDTD simulations show nanoring cavity and nanohole+disc arrays possess sharp Fano-like resonances in the visible spectral range. The much weaker resonances observed in experiments are resulted from the scattering loss of rough surfaces and fabrication imperfections. The resonance wavelengths of surface plasmons are strongly dependent on the periods of the arrays thus can be tuned near the working laser wavelength simply by varying the periods.[30]

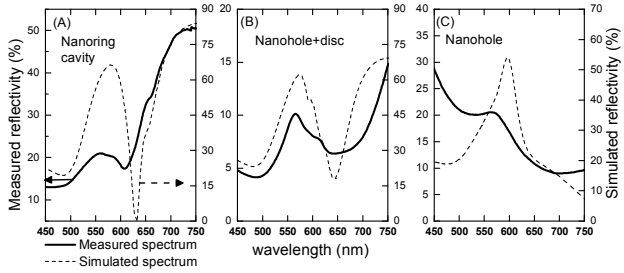

Fig. 3 Comparison of measured and simulated reflectivity from (A) nanoring cavity (B) nanohole+disc (C) nanohole arrays with 55-nm-thick gold deposition and 500 nm period. The measured and simulated spectra were read according to left and right axis in each figure.

Raman scattering experiments were carried out using a confocal Raman spectroscope (HR800). Each Raman spectrum was collected with an integration time of 20 seconds. The samples were immersed in 2×10^{-6} M solutions of rhodamine 6G (R6G). A 633 nm laser was chosen instead of a 520 nm laser for two reasons. The first reason is to avoid the effect of expected resonant Raman scattering (RRS) of R6G excited at 528 nm. The additional enhancement factor from RRS has been estimated to be 10^5 compared to non-resonant Raman scattering, which may distort the evaluations of AEF.[25,31] Secondly, the 633 nm wavelength falls on the band of surface plasmon resonance for the nanoring cavity and the nanohole+disc arrays as shown in the reflection spectrum (Fig. 3). Fig. 4(A) shows the Stokes-shifted Raman scattering spectra of R6G from the nanoring cavity templates with various thickness of gold deposition. The characteristic peaks of R6G can be clearly identified. The maximum Raman intensity is observed when the thickness of gold deposition is 55 nm as shown in Fig. 4(A). The AEF of nanoring cavity, nanohole+disc and nanohole arrays as a function of gold layer thicknesses were compared in Fig. 4(B). The estimation of AEF was based on the intensity of aromatic C-C stretching at 1360 cm^{-1}, which were averaged from 10 to 15 areas on each sample. The AEF of a nanoring cavity array displays a peak when the thickness of the gold layer increases to 55 nm, while those of nanohole and nanohole+disc arrays gradually approach to a saturated value when the thickness increases. The maximum AEF of the nanoring cavity arrays with various gold layer thicknesses is 1.3×10^5 and approximately 1-2 order higher than those of nanohole+disc and nanohole arrays with 1.5×10^4 and 5.5×10^3.

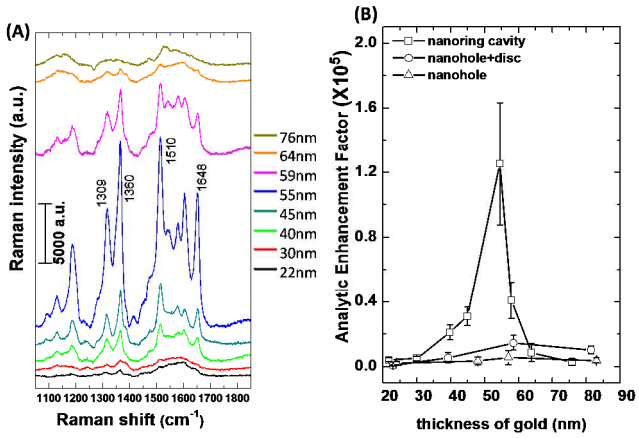

Fig. 4 (A) Stokes-shifted SERS spectra of R6G from the nanoring cavity arrays with different thickness of gold deposition. The intensity of aromatic C-C stretching at 1360 cm^{-1} is used for AEF calculation. (B) Comparison of the AEF

from nanoring cavity, nanohole+disc, and nanohole templates with different thickness of gold deposition. The maximum AEF of $1.3x10^5$ is observed from the nanoring cavity arrays when the thickness of gold deposition is 55 nm. The error bar is the standard deviation of measured SERS magnitudes from each set of measurements.

The different trends and magnitudes of AEFs from the three SERS substrates can be qualitatively understood by inspecting their structures. The upper panel of Fig. 5 demonstrates how the geometric complexities evolve from a nanohole, a nanohole+disc to a nanoring cavity by 3D cartoons of cross sectional view. The simplest structure among them is a nanohole. A nanohole + disc possesses an additional disc embedded inside a hole. As for a nanoring cavity, more nanostructures including a hole, a pillar and a ring are stacked within a unit cell, resulting in additional gaps, edges, and corners. Moreover, the plasmonic couplings between the nanostructures (a hole, a pillar and a ring) may result in stronger field enhancement.[32] The small areas with strongly enhanced fields are usually called "hot spots", which contribute to the large SERS effect. The field enhancement and hot spots distribution were simulated by the FDTD method. The geometric parameters used for the FDTD modeling were obtained from the SEM and the AFM measurements in order to access the real structure, which include the thickness of gold deposition equals to 55 nm, the period equals to 500 nm and the outer/inner diameters equal to 370 and 216 nm, and so on. The dielectric constant of the environment was taken as water and the grid was set to be 2 nm. The incident plane wave propagated along the negative Z direction with electric field polarized in X direction. Periodic boundary conditions were applied to X and Y directions while perfectly matched layer boundary conditions were applied to Z direction. The FDTD results shown in Fig. 5 clearly indicate that when excited by a laser with a wavelength of 633 nm, the nanoring cavity provides higher density of hot spots and larger field enhancement than the nanohole does. The FDTD simulation results are consistent with the experimental AEF, as illustrated in Fig. 4 and Fig. 5. From the above analysis, we suggest that the nanoring cavity array is a superior candidate as a SERS substrate compared with the nanohole array.

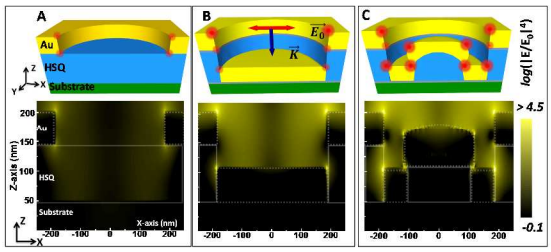

Fig. 5 Schematic diagrams (upper panels) and simulated field enhancement distributions (lower panels) of (A) a nanohole, (B) a nanohole+disc, and (C) a nanoring cavity unit cell in Z-X plane with thickness of gold equals to 55 nm. The colors of gold, dielectric HSQ, substrate and hot spots are presented as yellow, blue, green and red, respectively in schematic diagrams. The schematic hot spots are plotted mimicking the simulation results. The simulated field enhancement is displayed on a logarithmic scale. The E_0 and K are amplitude of electric field and wave vector of incident light with λ = 633 nm. The dashed and solid lines are added to indicate the gold and HSQ boundaries.

The influence of the gold layer thickness on AEF of nanoring cavity-templated SERS substrates must be taken into account. Fig. 4 shows the AEF of the nanoring cavity substrates first rise and then drops rapidly with the increasing gold layer thickness. The maximum value of AEF corresponds to 55 nm gold deposition. To explain this trend, let us inspect the cross sectional SEM images of nanoring cavities with different gold deposition as shown in the upper panels of Fig. 6(A) to (C). As the thickness of the gold layer increases from 20 nm to 55 nm, the volume of gold increases thus the gaps between nanostructures (holes, pillars and rings) are decreased. The smaller gaps can give rise to larger field enhancement due to the stronger plasmonic coupling between nanostructures.[15] The trend is verified by the FDTD simulations as shown in the lower panels of Fig. 6(A) and (B). We observe higher intensity of hot spots in Fig 6(B), corresponding to higher Raman intensity. The factor lowering the AEF in the stage of gold layer thickness ranging from 55-80 nm may be due to the lateral gold deposition. Thicker gold deposition will result in severe lateral deposition, which destroys the nanogaps and smooth the nanostructured surface. An example is taken from the SEM image of a nanoring cavity with 80-nm-thick gold layer (Fig. 6(C)). The severe lateral deposition blunts the boundaries between the pillar, the ring and the hole and subsequently brings to a flatter surface and continuous phase as shown in Fig. 6(C), resulting in a dramatic drop of AEF.

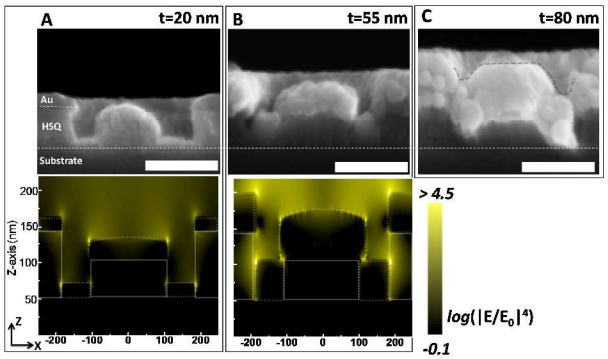

Fig. 6 Cross sectional SEM images of nanoring cavity architecture (upper panels) and the corresponding field enhancement distribution by FDTD simulations (lower panels) with (A) thickness of gold deposition = 20 nm, (B) 55 nm, and (C) 80 nm in the Z-X plane. The connected and blunted boundary of gold layer is indicated by a gray dashed line in the SEM image of (C). All scale bars in SEM images are 200 nm.

Based on the above results, we postulate that the nanoring cavity array has a considerable advantage in SERS performance over the nanohole array. However, the

maximum SERS enhancements have not been achieved for both nanohole and nanoring cavity arrays. There is evidence in the literature that supports the need for tuning the plasmon wavelength of the SERS substrate to match the laser wavelength as a favorable condition to achieve high sensitivity in detection.[33-35] To optimize the SERS enhancements, we tuned the plasmon bands to the laser wavelength by vary periods and gold thickness of arrays. The measured reflection spectra of arrays with 780 nm period and varied gold thickness are shown in Fig. 7(A). And the corresponding SEM images are shown in Fig. 7(B) and (C). The reflection spectra exhibit the features of Fano resonances, implying the existence of the coupling of LSPR and SPR[28,29]. In the spectrum of the nanoring cavity array consisting of a 50 nm gold layer, the broad resonance centered at 649 nm might be associated with LSPR, and the relatively sharp resonance centered at 698 nm is attributed to BW-SPP. The dashed line in Fig. 7(A) indicates the laser wavelength, which falls within the plasmon bands for both the nanoring cavity array and the nanohole array. Our results summarized in Table1 show that the maximum AEFs of the nanoring cavity arrays and the nanohole arrays are estimated to be about $3.1x10^5$ and $6.3x10^4$, respectively. The condition for maximum AEF occurs when the laser wavelength is located within the plasmon bands, as shown in Fig. 7(A). These results further support our suggestion that the nanoring cavity array has better SERS enhancement than the nanohole array possesses.

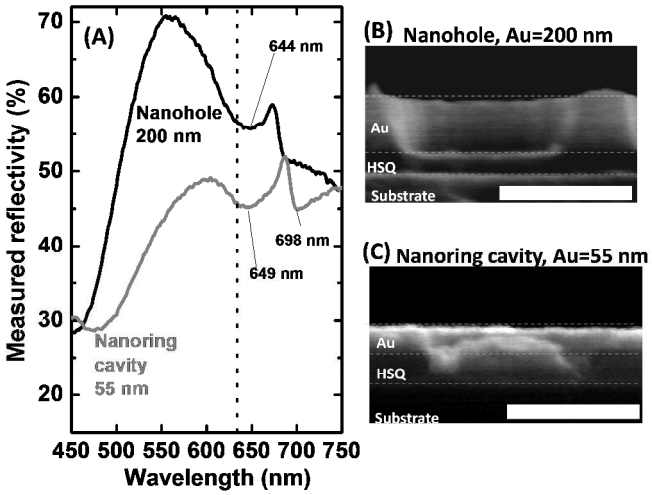

Fig. 7 (A) Reflection speatra of the nanohole array with 200-nm-thick gold (black) and the nanoring cavity array with 55-nm-thick gold (gray) measured in water. (B) and (C) are the cross-sectional SEM images of the nanoring cavity and the nanohole corresponding to (A). The scale bar is 500 nm. The dashed line in (A) signifies the laser wavelength of 633 nm.

Table 1 Summary of SERS performance.

Period (nm)	Geometry	outer/inner diameter(nm)	metal	thickness (nm)	AEF
500	nanohole	370/--	gold	55	5.5×10^3
780*	nanohole	645/--	gold	55	1.9×10^4
780	nanohole	645/--	gold	200	6.3×10^4
500	nanoring cavity	370/216	gold	55	1.3×10^5
780	nanoring cavity	645/317	gold	55	$3.1x10^5$

The reflection spectrum and SEM images of (*) are placed in section 5 of the supporting information.

Conclusion

In this study, we have developed a novel fabrication method for producing a Quasi-3D nanoring cavity array with advantages of low cost, large-area uniformity, and high SERS factor. The key fabrication to obtain a nanoring cavity array is simply by reversing the fabricating sequences of HCL. The optimal AEF of the nanoring cavity-templated substrate is considerably higher than that of conventional nanohole-based SERS substrates with similar dimensions. We verified that the better SERS performance of nanoring cavity arrays come from increased density of hot spots and stronger field enhancement than those of nanohole-based SERS substrates. We believe the nanoring cavity array with good SERS performance can serve as an alternative to those plasmonic sensing devices using nanohole arrays. The unique disc/ring-in-hole structure defined by NSL may provide potential plasmonic applications not only for SERS, but also in other areas such as photocatalysis, plasmonic solar cells and lab-on-chip sensing devices[36].

Experimental section

Fabrication of nanoring cavity. Cr/HSQ bilayers were coated on a silicon wafer (HSQ/Cr/Silicon). The first layer was 20-nm-thick Cr deposited by thermal evaporation and served as an etching barrier. HSQ (Dow Corning XR-1541) was diluted by dehydrated Methyl isobutyl ketone (MIBK) (1:3 by volume), purchased from J.T. Baker and filtrated through 200 nm pore size filter, followed by spin-casting on the etching barrier at 3000 rpm. The HSQ film was cured at 270 °C for 20 min and then cleaned by oxygen plasma. The long-range ordered PS NSs monolayer was then deposited on the HSQ surface using the air/water interfacial assembly. O_2 RIE (Plasmalab plus80) was applied to reduce the size of PS NSs at power = 50 watt, pressure = 50 mtorr, flow rate = 20

sccm and self-DC bias = 167 V. Subsequent 15 nm Cr was capped by thermal evaporation for etching mask. CF_4 RIE was then conducted to etch HSQ layer in the environment of 80 watt, 0.14 mbar, 40 sccm, self-DC bias 250 V and working time of 18 minutes. Different gold thicknesses were then deposited on the nanoring cavity through thermal evaporation. ***Fabrication of nanohole+nanodisc.*** The CF_4 etching recipe on HSQ layer masked by Cr (15 nm) for nanohole+nanodisc was the same as that in the fabrication of nanoring cavity except that the PS spheres were removed before etching. The etching time was 6 minutes. ***Fabrication of nanohole***. Cr (3 nm)/Au was thermal evaporated onto the reduced PS spheres array on HSQ/Cr/silicon substrate, followed by removal of spheres using scotch tape. ***Measurement of reflectivity.*** In order to understand the optical properties on our nanostructures, the inspection of plasmon bands were carried out by UV-Vis spectrometer (Jasco-v550) coupled with specular reflectance accessory. The white light which served as source was provided by a halogen lamp with wavelength ranging from 330 to 900 nm. The light was normally incident on the sample with a water covering surface. The reflection was collected against aluminum-deposited plane mirror (standard mirror). The planar Cr/HSQ/Silicon substrate was used as reference. ***Measurement of Raman scattering.*** Raman scattering measurements were carried out by a confocal microscope (Horiba Jobin Yvon) equipped with 17 mW HeNe laser (λ = 632.8 nm) and an objective lens (MPL×100). The scattered phonons were gathered by the same objective lens and introduced into holographic notch filter for blocking the Rayleigh scattering. The spectrum was acquired by a liquid-nitrogen cooled CCD. Detailed calculation of AEF is placed in the first section of supporting information.

FDTD Simulations. The FDTD simulations were performed with commercial software (Lumerical FDTD solution). The incident plane wave propagated along the negative Z direction with electric field polarized in X direction. The substrate was in the X-Y plane. Periodic boundary conditions were applied to X and Y directions while perfectly matched layer boundary conditions were applied to Z direction. The environment was taken as water and the grid was set to be 2 nm for all axes. The geometric parameters in simulation were obtained from SEM (Hitach S4200) and AFM (Park XE100) measurements in order to access real structure. Simulation time was set to be longer than 300 fs, which was long enough to ensure convergence.

* Address correspondence to
tylee63@gmail.com

ACKNOWLEDGMENT

The work was supported by the postdoctoral program (100N6807E1 and 101N1807E1) from National Tsing Hua University, Biomedical Engineering Program (NSC-101-2221-E-007-032-MY3), and Nanotechnology National program (NSC-101-2121-M-007-001-) from National Science Council, Taiwan, and research program on nanoscience and nanotechnology at Academia Sinica, Taipei, Taiwan.

Notes and references

(1) Fleischmann, M.; Hendra, P. J.; McQuillan, A. J. *Chemical Physics Letters* **1974**, *26*, 163.

(2) Xu, H.; Bjerneld, E. J.; Käll, M.; Börjesson, L. *Physical Review Letters* **1999**, *83*, 4357.

(3) Kneipp, K.; Wang, Y.; Kneipp, H.; Perelman, L. T.; Itzkan, I.; Dasari, R. R.; Feld, M. S. *Physical Review Letters* **1997**, *78*, 1667.

(4) Xu, H.; Aizpurua, J.; Käll, M.; Apell, P. *Physical Review E* **2000**, *62*, 4318.

(5) Li, Q.; Jiang, Y.; Han, R.; Zhong, X.; Liu, S.; Li, Z.-Y.; Sha, Y.; Xu, D. *Small* **2012**, n/a.

(6) Liu, T.-Y.; Tsai, K.-T.; Wang, H.-H.; Chen, Y.; Chen, Y.-H.; Chao, Y.-C.; Chang, H.-H.; Lin, C.-H.; Wang, J.-K.; Wang, Y.-L. *Nat Commun* **2011**, *2*, 538.

(7) Bahns, J. T.; Guo, Q.; Montgomery, J. M.; Gray, S. K.; Jaeger, H. M.; Chen, L. *The Journal of Physical Chemistry C* **2009**, *113*, 11190.

(8) Anker, J. N.; Hall, W. P.; Lyandres, O.; Shah, N. C.; Zhao, J.; Van Duyne, R. P. *Nat Mater* **2008**, *7*, 442.

(9) Masson, J.-F.; Murray-Methot, M.-P.; Live, L. S. *Analyst* **2010**, *135*, 1483.

(10) Caldwell, J. D.; Glembocki, O.; Bezares, F. J.; Bassim, N. D.; Rendell, R. W.; Feygelson, M.; Ukaegbu, M.; Kasica, R.; Shirey, L.; Hosten, C. *ACS Nano* **2011**, *5*, 4046.

(11) Brolo, A. G.; Arctander, E.; Gordon, R.; Leathem, B.; Kavanagh, K. L. *Nano Letters* **2004**, *4*, 2015.

(12) Valsecchi, C.; Brolo, A. G. *Langmuir* **2013**, *29*, 5638.

(13) Yu, Q.; Guan, P.; Qin, D.; Golden, G.; Wallace, P. M. *Nano Letters* **2008**, *8*, 1923.

(14) Banaee, M. G.; Crozier, K. B. *Opt. Lett.* **2010**, *35*, 760.

(15) Wei, H.; Håkanson, U.; Yang, Z.; Höök, F.; Xu, H. *Small* **2008**, *4*, 1296.

(16) Li, X.; Zhang, Y.; Shen, Z. X.; Fan, H. J. *Small* **2012**, *8*, 2548.

(17) Huang, F. M.; Wilding, D.; Speed, J. D.; Russell, A. E.; Bartlett, P. N.; Baumberg, J. J. *Nano Letters* **2011**, *11*, 1221.

(18) Stewart, M. E.; Mack, N. H.; Malyarchuk, V.; Soares, J. A. N. T.; Lee, T.-W.; Gray, S. K.; Nuzzo, R. G.; Rogers, J. A. *Proceedings of the National Academy of Sciences* **2006**, *103*, 17143.

(19) Wei, H.; Xu, H. *Nanoscale* **2013**, *5*, 10794.

(20) Im, H.; Bantz, K. C.; Lee, S. H.; Johnson, T. W.; Haynes, C. L.; Oh, S.-H. *Advanced Materials* **2013**, n/a.

(21) Nordlander, P. *ACS Nano* **2009**, *3*, 488.

(22) Hao, F.; Nordlander, P.; Sonnefraud, Y.; Dorpe, P. V.; Maier, S. A. *ACS Nano* **2009**, *3*, 643.

(23) Atwater, H. A.; Polman, A. *Nat Mater* **2010**, *9*, 205.

(24) Burgos, S. P.; de Waele, R.; Polman, A.; Atwater, H. A. *Nat Mater* **2010**, *9*, 407.

(25) Le Ru, E. C.; Blackie, E.; Meyer, M.; Etchegoin, P. G. *The Journal of Physical Chemistry C* **2007**, *111*, 13794.

(26) Xu, J.; Kvasni?ka, P.; Idso, M.; Jordan, R. W.; Gong, H.; Homola, J. í.; Yu, Q. *Opt. Express* **2011**, *19*, 20493.

(27) Fredriksson, H.; Alaverdyan, Y.; Dmitriev, A.; Langhammer, C.; Sutherland, D. S.; Zäch, M.; Kasemo, B. *Advanced Materials* **2007**, *19*, 4297.

(28) Prodan, E.; Radloff, C.; Halas, N. J.; Nordlander, P. *Science* **2003**, *302*, 419.

(29) Lee, K.-L.; Chen, P.-W.; Wu, S.-H.; Huang, J.-B.; Yang, S.-Y.; Wei, P.-K. *ACS Nano* **2012**, *6*, 2931.

(30) Chang, S.-H.; Gray, S.; Schatz, G. *Opt. Express* **2005**, *13*, 3150.

(31) Jensen, L.; Schatz, G. C. *The Journal of Physical Chemistry A* **2006**, *110*, 5973.

(32) Tong, L.; Wei, H.; Zhang, S.; Li, Z.; Xu, H. *Physical Chemistry Chemical Physics* **2013**, *15*, 4100.

(33) Félidj, N.; Aubard, J.; Lévi, G.; Krenn, J. R.; Salerno, M.; Schider, G.; Lamprecht, B.; Leitner, A.; Aussenegg, F. R. *Physical Review B* **2002**, *65*, 075419.

(34) Haynes, C. L.; Van Duyne, R. P. *The Journal of Physical Chemistry B* **2003**, *107*, 7426.

(35) McFarland, A. D.; Young, M. A.; Dieringer, J. A.; Van Duyne, R. P. *The Journal of Physical Chemistry B* **2005**, *109*, 11279.

(36) Rissin, D. M.; Kan, C. W.; Campbell, T. G.; Howes, S. C.; Fournier, D. R.; Song, L.; Piech, T.; Patel, P. P.; Chang, L.; Rivnak, A. J.; Ferrell, E. P.; Randall, J. D.; Provuncher, G. K.; Walt, D. R.; Duffy, D. C. *Nat Biotech* **2010**, *28*, 595.